1 **Evidence for the interior evolution of Ceres from geologic analysis of fractures**

2

3 **J. E. C. Scully[1]*, D. L. Buczkowski[2], N. Schmedemann[3], C. A. Raymond[1], J. C. Castillo-**

4 **Rogez[1], S. D. King[4], M. T. Bland[5], A. I. Ermakov[1], D. P. O'Brien[6], S. Marchi[7], A.**

5 **Longobardo[8], C. T. Russell[9], R. R. Fu[10], and M. Neveu[11].**

6

7 [1]Jet Propulsion Laboratory, California Institute of Technology, 4800 Oak Grove Drive,

8 Pasadena, California 91109, USA, [2]Johns Hopkins University Applied Physics Laboratory,

9 Laurel, Maryland 20723, USA, [3]Freie Universität Berlin, 12249 Berlin, Germany, [4]Virginia

10 Tech, Blacksburg, Virginia 24061, USA, [5]US Geological Survey, Astrogeology Science Center,

11 Flagstaff, Arizona 86001, USA, [6]Planetary Science Institute, Tucson, Arizona 85719, USA,

12 [7]Southwest Research Institute, Boulder, Colorado 80305, USA, [8]INAF Istituto di Astrofisica e

13 Planetologia Spaziali (IAPS), 00133 Rome, Italy, [9]Department of Earth, Planetary, and Space

14 Science, University of California, Los Angeles, California 90095, USA, [10]Lamont-Doherty Earth

15 Observatory, Columbia University, Palisades, New York 10964, USA, [11]Arizona State

16 University, Tempe, AZ 85287, USA.

17

18 *Corresponding author: Jennifer E. C. Scully (jennifer.e.scully@jpl.nasa.gov)

19

20 **Key Points:**

21 • We identify all ≥ 1 km wide linear features outside impact craters: most are secondary

22   crater chains and there is one set of pit chains.

23 • Pit chains are the surface expression of subsurface fractures and they reveal the localized

24 outer layer is thicker than Ceres' average.

25 • We propose a region of upwelling material, resulting from convection/diapirism, formed

26 the pit chains and we derive its characteristics.

27

28

29

30

31

32

33

34

35

36

37

38

39

40

41

42

43 **Abstract**

44 Ceres is the largest asteroid-belt object and has been observed by the Dawn spacecraft since

45 2015. Dawn observed two morphologically distinct linear features on Ceres' surface: secondary

46 crater chains and pit chains. Pit chains provide unique insights into Ceres' interior evolution. Pit

47 chains called the Samhain Catenae are interpreted as the surface expression of subsurface

48 fractures. Using their spacing, we estimate that the localized thickness of Ceres' fractured, outer

49 layer is approximately ≥58 km, at least ~14 km greater than average. We hypothesize that the

50 Samhain Catenae were formed by extensional stresses induced by a region of upwelling material

51 resulting from convection/diapirism. We derive characteristics for this upwelling material that

52 can be used as constraints in future interior modeling studies. For example, its predicted location

53 coincides with Hanami Planum, a high-elevation region with negative residual gravity anomaly,

54 which may be surficial evidence for this proposed region of upwelling material.

55 **1. Introduction**

56   Prior to the Dawn mission [*Russell et al.,* 2016], dwarf planet Ceres (radius ~470 km)

57 was studied via telescopic observations and modeling investigations. Telescopic observations

58 allowed for the initial determination of Ceres' dimensions and average bulk density, and

59 provided evidence for at least partial differentiation [*Thomas et al.*, 2005; *Drummond et al.*

60 2014]. Thermal evolution models predicted Ceres differentiated into a rocky interior and a 50-

61 100 km thick water-ice-dominated outer layer [*Castillo-Rogez and McCord,* 2010; *McCord and*

62 *Sotin,* 2005], within which extensive viscous relaxation was predicted to occur [*Bland,* 2013].

63 Alternatively, arguments were also made for an undifferentiated interior [*Zolotov,* 2009].
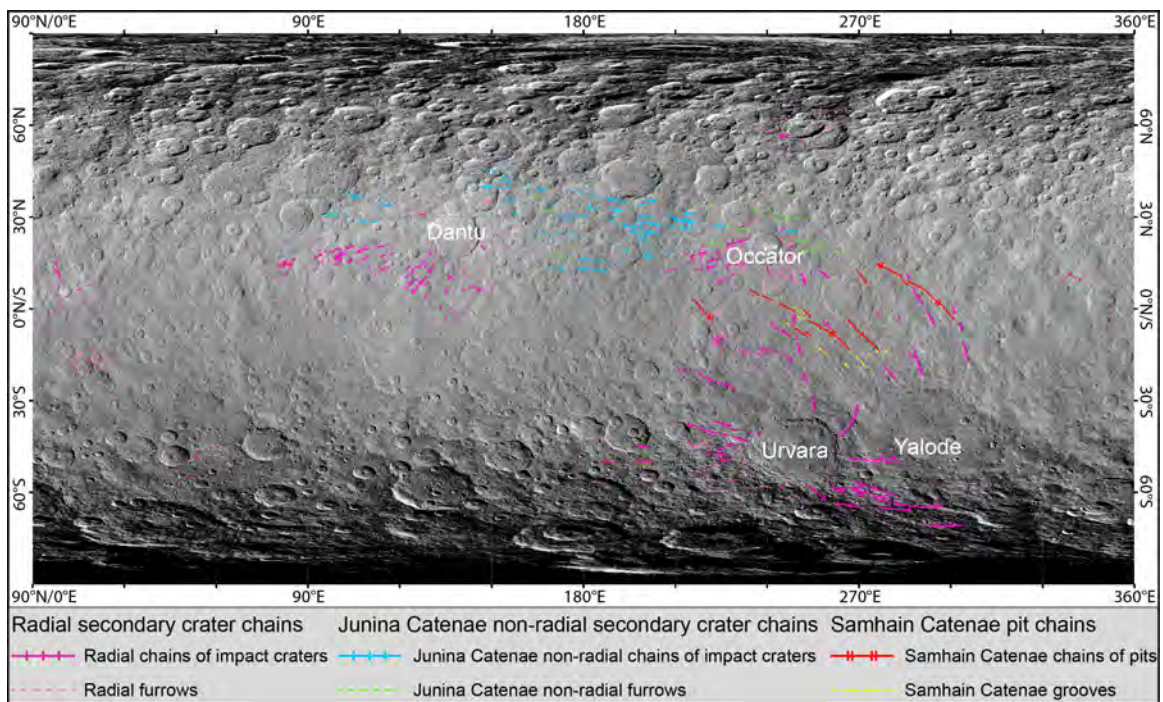
64   A deeper understanding of Ceres' interior required orbital observations, which were

65 provided by Dawn and refine Ceres' dimensions and bulk density [*Russell et al.,* 2016]. They

66   also indicate partial differentiation into a rock-rich interior and an outer layer that is

67   comparatively enriched in volatiles [*Park et al.,* 2016]. Dawn obtained images with two to three

68   orders of magnitude higher resolution than previous telescopic observations: ≥35 m/pixel

69   [*Buczkowski et al.,* 2016] versus 30 km/pixel [*Li et al.,* 2006]. These images reveal a heavily

70   cratered surface [*Hiesinger et al.,* 2016; *Marchi et al.,* 2016] that is inconsistent with the

71   predicted extensive surficial viscous relaxation [*Bland,* 2013]. Furthermore, the surface

72   morphology and finite element modeling indicate Ceres' outer layer is a mixture of <30-40% of

73   a weak phase (water ice and porosity) and >60-70% rock/salts/clathrates [*Buczkowski et al.,*

74   2016; *Bland et al.,* 2016]. Dawn's high-resolution images also show numerous linear features on

75   Ceres' surface [*Buczkowski et al.,* 2016].

2. Types of linear features and ejecta distribution

77   We investigate these linear features by producing a global map of all linear features that

78   are ≥1 km wide and are outside of impact craters. The global map contains 2,319 individual

79   segments and is based on images from Dawn's Framing Camera and the shape model of Ceres

80   [*Roatsch et al.,* 2016; *Preusker et al.,* 2016] (Text S1-S2) (Figures 1, S1-S2). Using this global

81   map, we identify two types of linear features: secondary crater chains and pit chains. While we

82   use the pit chains to gain insights into Ceres' interior evolution, it is also necessary to study the

83   secondary crater chains, to ensure that pit chains are not misidentified as secondary crater chains,

84   and vice versa. We distinguish between the secondary crater chains and pit chains using the

85   following morphologic characteristics. Secondary craters have more clearly defined rims and

86   more regular shapes in comparison to the pits, and the chains of secondary craters are often

87   (though not always) located in a radial pattern around a source impact crater. These

88   characteristics are consistent with the formation of the secondary crater chains by the impact and

89   scour of material ejected during the formation of a central source impact crater (Text S3) (Figure

90   2). In contrast, the pits have poorly defined rims and more irregular shapes than the secondary

91   craters, and the chains of pits are not located in a radial pattern around an impact crater. These

92   characteristics are indicative of the pit chains forming by drainage of material into a subsurface

93   void, and are analogous to pit chains on other bodies [*Wyrick et al.,* 2004; *Buczkowski et al.,*

94   2008; *Ferrill et al.,* 2011; *Scully et al.,* 2014; *Martin et al.,* 2017] (Text S6) (Figure 2). The

95   secondary crater chains and pit chains also display different behaviors in color and spectral data

96   [*De Sanctis et al.,* 2015], which is similar to other bodies [*Longobardo et al.,* 2015] (Text S7).

98   **Figure 1.** Global map of prominent linear features, classified by interpretation into radial

99   secondary crater chains, Junina Catenae non-radial secondary crater chains and Samhain Catenae

100   pit chains. Their sub-divisions are discussed in Text S2, S3 and S6 and in Figure 2. Impact

101   craters discussed in the text are labeled. The basemap is an equirectangular projection of the

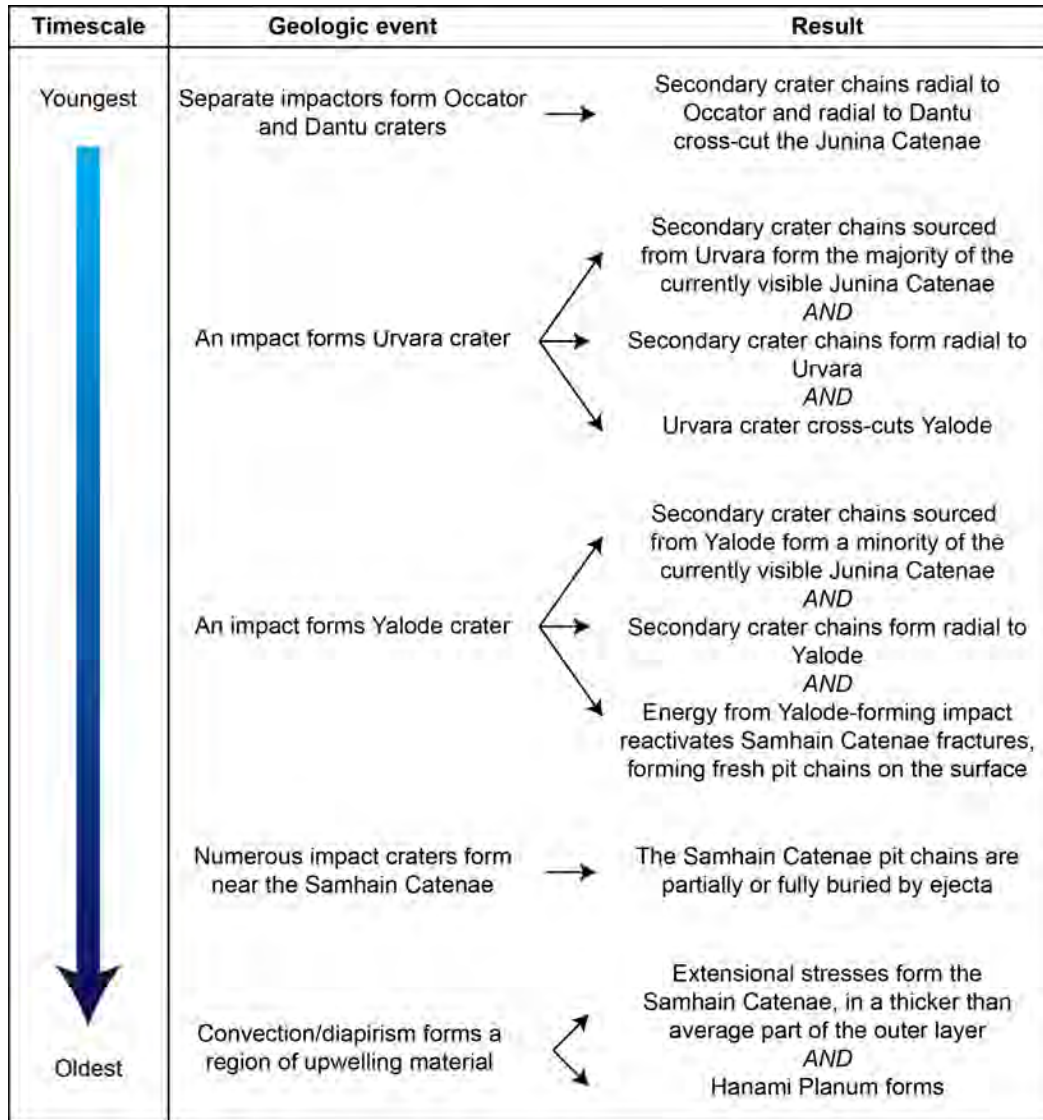102   Framing Camera LAMO clear filter global mosaic (35 m/pixel) (Text S1).

103
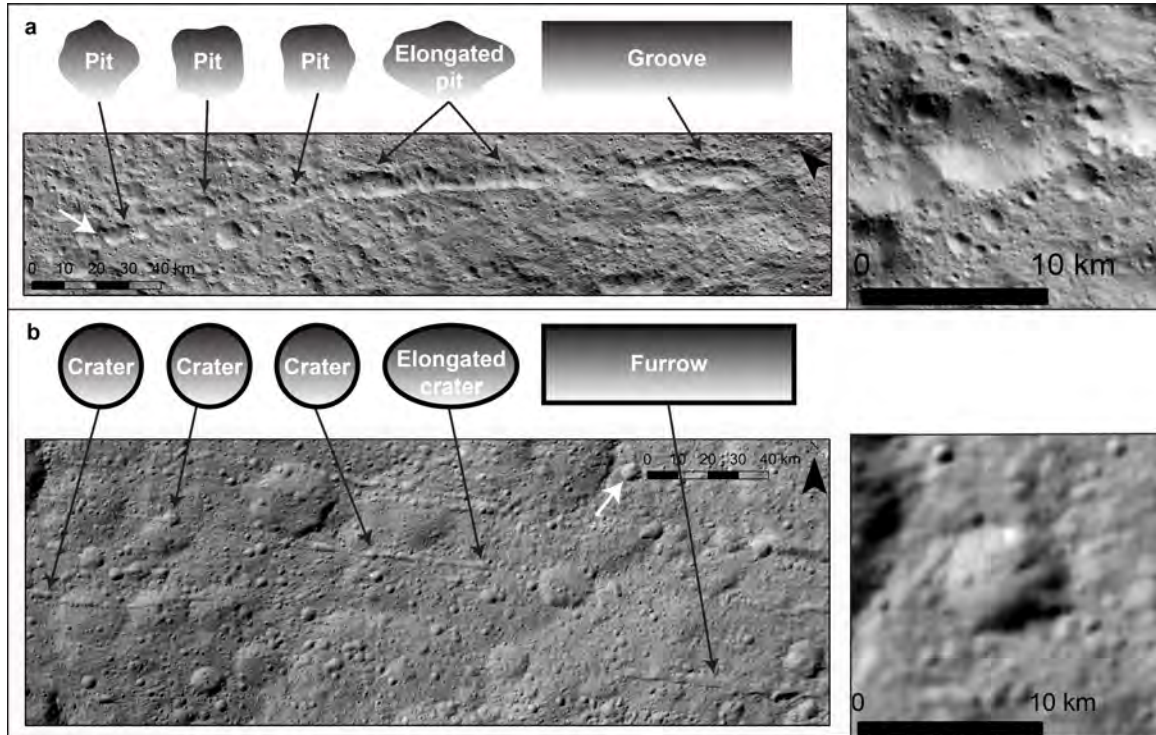
Figure 2. Schematic illustrations and examples of (**a**) pit chains and (**b**) secondary crater chains. Pit chains are made up of grooves (elongated pits) and chains of pits, which have more poorly defined rims and more irregular shapes than secondary craters (Text S2 and S6). (**b**) Secondary crater chains are made up of furrows (elongated impact craters) and chains of impact craters, which have more clearly defined rims and more regular shapes than pits (Text S2-S3). White arrows indicate the locations of the detailed images (right).

The majority of the linear features are radial secondary crater chains, which surround thirteen source impact craters. Those around Occator, Dantu and Urvara craters are the most prominent (Figures 1, S3-S4). However, one set of secondary crater chains, named the Junina Catenae, are not radial to a source impact crater. They are located from ~12-46°N and ~95-265°E, are oriented ~WNW-ESE, and consist of ~11 secondary crater chains that fan out to the west (Figures 1 and S5). Their average length is 491 km, their maximum/minimum widths are 4

118   km/1 km, their average depth is 230 m and their average spacing is 22 km. The Junina Catenae

119   are cross-cut by, and thus older than, Occator and Dantu craters and their associated radial

120   secondary crater chains (Figures 1, 3 and S5).

121

Timescale	Geologic event	Result
Youngest	Separate impactors form Occator and Dantu craters	Secondary crater chains radial to Occator and radial to Dantu cross-cut the Junina Catenae
	An impact forms Urvara crater	Secondary crater chains sourced from Urvara form the majority of the currently visible Junina Catenae *AND* Secondary crater chains form radial to Urvara *AND* Urvara crater cross-cuts Yalode
	An impact forms Yalode crater	Secondary crater chains sourced from Yalode form a minority of the currently visible Junina Catenae *AND* Secondary crater chains form radial to Yalode *AND* Energy from Yalode-forming impact reactivates Samhain Catenae fractures, forming fresh pit chains on the surface
	Numerous impact craters form near the Samhain Catenae	The Samhain Catenae pit chains are partially or fully buried by ejecta
Oldest	Convection/diapirism forms a region of upwelling material	Extensional stresses form the Samhain Catenae, in a thicker than average part of the outer layer *AND* Hanami Planum forms

122   **Figure 3.** Timeline showing key events discussed in this work, from youngest to oldest. The

123   details are discussed in the text.

124

125   An ejecta distribution model explains how material ejected from Urvara crater, in the

126   southern hemisphere, formed the Junina Catenae in the northern hemisphere [*Schmedemann et*

127 *al.,* 2017] (Text S4). This model predicts that because of Ceres' low gravity (0.27 m/s^2), material

128 ejected at ~45° and at high velocities from Urvara (~390-520 m/s) will travel above Ceres'

129 surface for a relatively long time (~6-8 hours). In comparison to bodies like the Earth, Ceres'

130 rotation period is short (~9 hours) and it is small (radius ~470 km) [*Russell et al.,* 2016]. Thus,

131 by the time this material impacts the surface to form the Junina Catenae, the surface underneath

132 it has rotated significantly, resulting in the material being located far from Urvara in a non-radial

133 pattern. The model predictions of the location, orientation and fan pattern of this high velocity

134 material is consistent with our mapping of the Junina Catenae (Figure 4). A minority of the

135 currently visible Junina Catenae may have been formed by the impact of material originating

136 from Yalode crater, which is adjacent to, and older than, Urvara (Text S5). Also consistent with

137 our mapping, the model predicts that material ejected at lower velocities from Urvara will form

138 radial secondary crater chains (Text S5) (Figure S3). We also map additional, unnamed sets of

139 secondary crater chains that are not oriented radially around a source impact crater (Figure S2).

140 We propose that these sets formed by the same process as the Junina Catenae, but that they have

141 different source craters. Ejecta distribution modeling has not yet been performed to identify their

142 source craters.
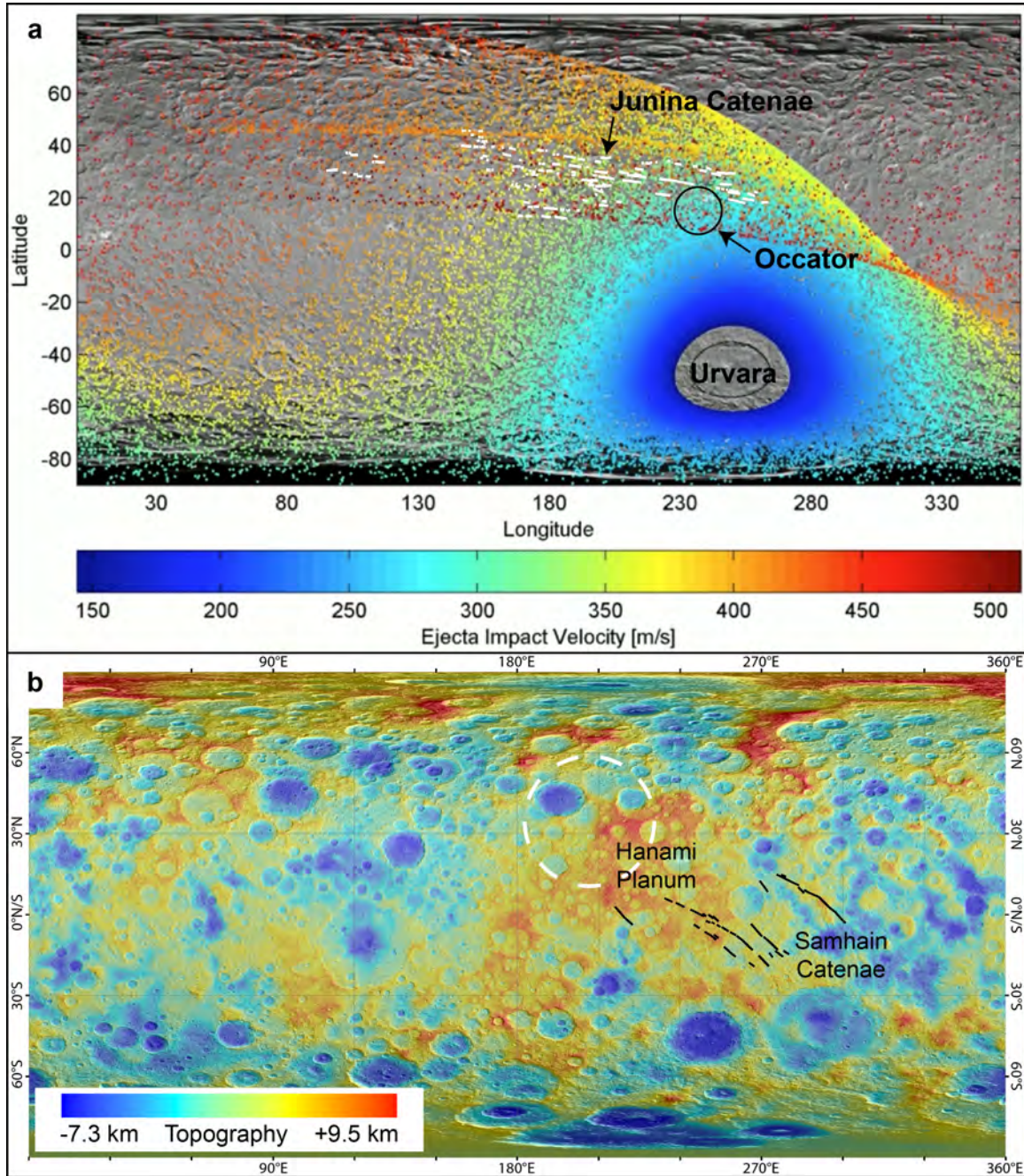
Figure 4. Formation of the Junina Catenae and Samhain Catenae. (**a**) Comparison between the

predicted distribution of high velocity material ejected from Urvara [*Schmedemann et al.,* 2017]

(red-orange dots) and our Junina Catenae mapping (white lines). (**b**) Locations of the Samhain

Catenae (black lines), Hanami Planum and the proposed region of upwelling material (white
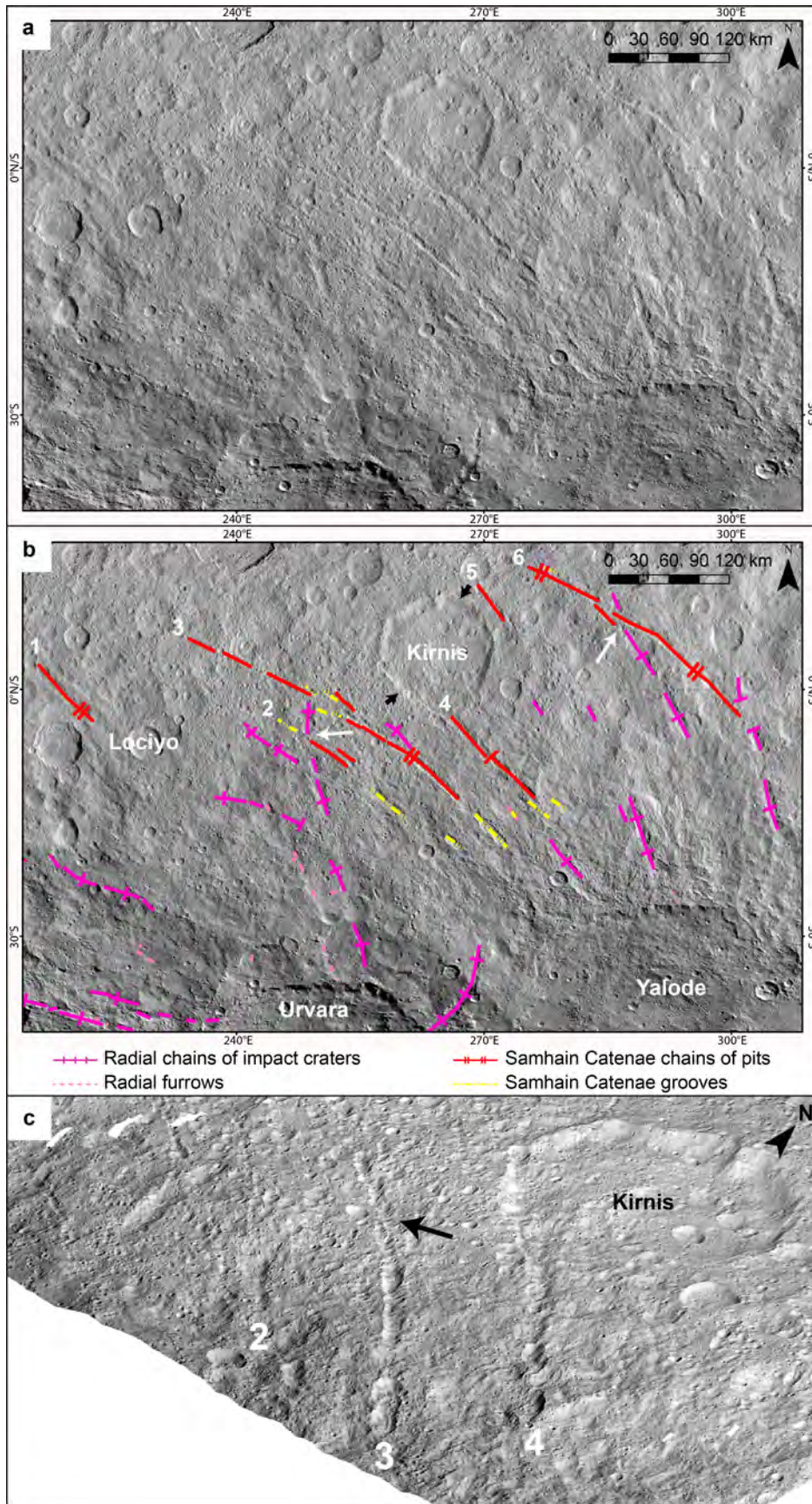
148   dashed circle). The basemap is the shape model overlain onto an equirectangular projection of

149   the Framing Camera LAMO clear filter global mosaic (Text S1).

150

151   **3. Samhain Catenae fractures and thickness of Ceres' outer layer**

152   Another set of linear features, called the Samhain Catenae, are also not radial to a source

153   impact crater (Figures 1 and 5). Unlike the Junina Catenae, we and *Buczkowski et al.* [2016]

154   interpret that the Samhain Catenae are not secondary crater chains that originate from Urvara

155   and/or Yalode, because they display the aforementioned morphological characteristics of pit

156   chains (Text S6) (Figure 2). Additionally, the Samhain Catenae are aligned to the straight rims of

157   polygonal craters, whose straight sides are hypothesized to be controlled by subsurface fractures

158   [*Buczkowski et al.,* 2016] (Figure 5). Moreover, we observe that the Samhain Catenae are cross-

159   cut by Urvara's and Yalode's secondary crater chains, indicating that they formed prior to

160   Urvara and Yalode (Figures 3 and 5).

161   The Samhain Catenae are oriented ~NW-SE between Occator and Urvara/Yalode craters

162   (Figure 1). They consist of ~6 discontinuous pit chains, with an average length of 202 km, a

163   maximum/minimum width of 11 km/5 km and an average depth of 1.1 km (Figure 5). The

164   Samhain Catenae are the only set of ≥1 km wide pit chains we identify on Ceres. Consistent with

165   analogous pit chains on other bodies [*Wyrick et al.,* 2004; *Buczkowski et al.,* 2008; *Ferrill et al.,*

166   2011; *Scully et al.,* 2014; *Martin et al.,* 2017], we interpret that the Samhain Catenae pit chains

167   are the surface expression of subsurface voids at depth. In this scenario, surficial material

168   draining into a subsurface void forms a funnel-like shape in cross-section, which appears as a pit

169   at the surface. We further interpret that extension fractures form these subsurface voids (Text

170   S6).

Radial chains of impact craters   Samhain Catenae chains of pits
Radial furrows   Samhain Catenae grooves

172 **Figure 5.** Samhain Catenae pit chains in (**a**) unmapped, (**b**) mapped and (**c**) perspective views.

173 (**b**) White arrows show example locations where Urvara/Yalode radial secondary crater chains

174 cross-cut the Samhain Catenae pit chains, which are labeled #1-6. Short black arrows indicate the

175 polygonal crater Kirnis' straight rims, which align with the Samhain Catenae. Kirnis' southern

176 straight rim merges with Samhain Catenae #4. The basemap is an equirectangular projection of

177 the Framing Camera LAMO clear filter global mosaic (Text S1). (**c**) Samhain Catenae #2-4 and

178 an example en-echelon pattern/S-shaped linkage (black arrow) (Text S6).

179

180   The spacing of tectonic features on planetary bodies is often used to estimate the

181 thicknesses of the layers in which they occur [e.g. *Gioia et al.*, 2007; *Yin et al.*, 2016; *Bland and*

182 *McKinnon*, 2015]. Numerical modeling and experiments show that the ratio of extension fracture

183 spacing to fractured layer thickness for fractures that have reached, or are near to, the level of

184 saturation is ~0.8-1.2 [*Bai and Pollard,* 2000]. The Samhain Catenae fractures, as indicated by

185 the pit chains at the surface, are likely near to saturation because their spacing is relatively

186 regular (Figure 5). The spacing between pit chains #1-2 is ~135 km, #2-3 is ~48 km, #3-4 is ~51

187 km, #4-5 is ~104 km and #5-6 is ~104 km. It is possible that additional fractures exist in the

188 subsurface, located centrally between #1-2, #4-5 and #5-6, which would result in a regular

189 spacing of ~50 km between all the fractures. Pit chains associated with these additional

190 subsurface fractures could have been concealed or erased from the surface by superposing

191 impact craters and their ejecta, such as Lociyo and Kirnis (Figure 5). However, because there is

192 no surficial morphological evidence for these additional subsurface fractures, in our calculations

193 we only use the spacings of the pit chains that are observed at the surface. Using the mean and

194 standard deviation of these spacings, and the aforementioned ratio of fracture spacing to

195   fractured layer thickness (~0.8-1.2), we estimate that the thickness of Ceres' fractured, outer

196   layer in the localized region around the Samhain Catenae is ~58-134 km.

197   Estimates of Ceres' globally averaged outer layer thickness have been derived from

198   interior models based on Dawn's gravity observations: $41.0^{+3.2}_{-4.7}$ km [*Ermakov et al.,* in

199   revision; *Fu et al.,* in revision] and 43-50 km [*Mitri et al.,* in revision]. In contrast, our outer

200   layer thickness estimate is only applicable to the vicinity of the Samhain Catenae. Thus, our

201   results suggest that Ceres' outer layer in this region is thicker than the global average. This is

202   consistent with *Ermakov et al.* [in revision], who suggest the outer layer is thickest in a region

203   called Hanami Planum. The Samhain Catenae are located on and adjacent to Hanami Planum

204   (Figure 4). By minimizing the power of the Bouguer anomaly, *Ermakov et al.* [in revision]

205   estimate that the outer layer is ~55 km thick at Hanami Planum. This is comparable to our lower

206   estimate of the outer layer thickness (~58 km). A regional outer layer thickness of ~58 km would

207   be consistent with our aforementioned suggestion that there are additional subsurface fractures

208   spaced at ~50 km. Thus, we interpret that our lower estimate, ~58 km, is most representative of

209   Ceres' outer layer thickness in the vicinity of the Samhain Catenae. The gravity-derived outer

210   layer thickness estimates reflect density differences between the outer layer and the underlying

211   material, while our fracture-derived estimate reflects a rheology/strength difference. Therefore,

212   the consistency between these outer layer thickness estimates in the vicinity of the Samhain

213   Catenae suggests that the density and rheology/strength boundaries between the outer layer and

214   underlying material occur at approximately the same depth in this region.

215   **4. Reactivation and formation of the Samhain Catenae**

216   Cross-cutting relationships indicate that Urvara and Yalode formed after the Samhain

217   Catenae, and that Yalode is older than Urvara (Figures 3 and 5). It is likely that geologic events

218   after the Samhain Catenae fractures' formation, such as the deposition of ejecta from impact

219   craters, would have partially or fully erased the initial pit chains from Ceres' surface. However,

220   the observation that the Samhain Catenae pit chains closer to Yalode are deeper than the further

221   pit chains (Figure S6) suggests that the large Yalode impact (260-km-diameter) reactivated the

222   Samhain Catenae fractures. Reactivating/reopening the fractures at depth would result in new

223   surficial material draining into the fractures, forming fresh pit chains on the surface that are

224   visible as the Samhain Catenae today. The nearby 170-km-diameter Urvara crater could also

225   have contributed to this reactivation.

226   Here we investigate three hypotheses for the formation of the Samhain Catenae being

227   induced by: (1) a basin-forming impact, (2) freezing of a global subsurface ocean, or (3) a region

228   of upwelling material. There is a geometric relationship between the Samhain Catenae and a

229   putative relict impact basin at 20°N, 340°E [*Marchi et al.,* 2016], suggesting that stresses derived

230   from the impact basin's formation could have initially formed the Samhain Catenae fractures.

231   However, the geometric correlation is weak and the identification of this impact basin is

232   ambiguous. Consequently, in agreement with *Buczkowski et al.* [2016], this is not our favored

233   formation mechanism of the Samhain Catenae.

234   Alternatively, freezing of a global subsurface ocean could have formed the Samhain

235   Catenae. In this scenario, the freezing ocean adds ice to the overlying outer layer, thickening and

236   inducing tensile stresses in the outer layer [*O'Brien et al.,* 2015; *Nimmo,* 2004; *Manga and*

237   *Wang,* 2007]. Dawn data indicate that Ceres' outer layer is mixture of water ice, rock, salts

238   and/or clathrates [*Hiesinger et al.,* 2016; *Bland et al.,* 2016; *Castillo-Rogez et al.,* 2016]. We

239   infer that such a mixture's tensile strength, without pre-existing weaknesses such as fractures, is

240   at least an order of magnitude higher than pure water ice (≥10 MPa versus ~0.01-1 MPa),

241   because the tensile strength of water ice-silicate particle mixtures is ~2-22 MPa [*Petrovic,* 2003;

242   *Lange and Ahrens,* 1983]. To fracture an outer layer with a tensile strength of ≥10 MPa,

243   thickening of ≥10 km [*O'Brien et al.,* 2015] would be required, which could have occurred

244   during freezing of a global subsurface ocean [*Castillo-Rogez et al.,* 2016]. However, if the

245   Samhain Catenae fractures formed as a result of this freezing, we would expect them to be

246   globally distributed, as on icy satellites [e.g. *Nimmo,* 2004; *Manga and Wang,* 2007]. It is

247   possible that globally distributed fractures are buried on Ceres, and that only the Samhain

248   Catenae portion were reactivated, and are hence visible today. However, there are approximately

249   a dozen large impact craters (>100 km), in addition to Yalode (260-km-diameter) and Urvara

250   (170-km-diameter), and none appear to have reactivated fractures. In particular, we would expect

251   Kerwan crater's formation (280-km-diameter) to have reactivated other portions of any globally

252   distributed fracture set. However, we find no pit chains of a similar scale to the Samhain Catenae

253   elsewhere on Ceres. This suggests that globally distributed fractures are not present, and

254   therefore, this is also not our favored formation mechanism of the Samhain Catenae.

255   The final hypothesis is that a region of upwelling material induced the Samhain

256   Catenae's formation. Multiple interior evolution models predict convection approximately within

257   Ceres' first billion years [*King et al.,* 2016; *Neveu and Desch,* 2015; *Travis and Feldman,* 2016].

258   Some models predict that convection continued after Ceres' first billion years, initially in the

259   liquid state and perhaps later in the solid state [*Neveu and Desch,* 2015; *Travis and Feldman,*

260   2016]. Additionally, upwelling of salt diapirs is proposed to occur in the geologically recent past

261   [*Buczkowski et al.,* 2016]. Thus, we hypothesize that a region of upwelling material derived from

262   one of these instances of convection/diapirism induced extensional stresses within a particular

263   portion of Ceres' outer layer, and formed the Samhain Catenae. Further modeling studies are

264   needed to evaluate this hypothesis, and our analysis of the Samhain Catenae provides predictions

265   about the proposed region of upwelling material's characteristics, which can be used as

266   constraints by future interior modeling studies.

5. Characteristics of the proposed region of upwelling material

268   The proposed upwelling would have occurred before Urvara's and Yalode's formation,

269   because we find that the Samhain Catenae are older than both craters. Additionally, the

270   upwelling material would need to induce extensional stresses within Ceres' outer layer that are

271   greater than our previously approximated value of the outer layer's tensile strength (≥10 MPa).

272   Furthermore, to form the Samhain Catenae, the extensional stresses induced in Ceres' outer layer

273   would need to be approximately perpendicular to the Samhain Catenae's current orientation.

274   Dike swarms are often used to locate terrestrial mantle plumes because their patterns are

275   indicative of the plume's location [*Ernst and Buchan,* 2001] (Figure S7). A dike is essentially a

276   fracture that is infilled with material, and both are formed by tensile stresses/extension.

277   Therefore, if the proposed region of upwelling material did form the Samhain Catenae, we can

278   use the patterns of dikes formed by mantle plumes on Earth as analogs to the pattern of the

279   Samhain Catenae, and thus approximate the location of the proposed region of upwelling

280   material. Dikes/fractures with a linear pattern are approximately parallel to one another, have a

281   higher density nearer to the upwelling material and their average thickness increases with

282   distance from the upwelling material [*Ernst and Buchan,* 2001] (Figure S7). The Samhain

283   Catenae are approximately parallel to one another, there are six pit chains in their northern half

284   and four in their southern half (Figure S6), and by measuring the widths of the pit chains at

285   regular intervals, we find that the average widths of five of the six pit chains are greatest at their

286   southern ends. Therefore, we find that the Samhain Catenae have a linear pattern, which is

287   consistent with the proposed region of upwelling material being located adjacent to the

288   northwestern end of the Samhain Catenae, at ~36°N, ~207°E (Figure 4).

289   **6. Conclusions**

290   Through our detailed analysis of Ceres' linear features, we find that the Samhain Catenae

291   are the only ≥1 km wide pit chains on Ceres' surface. The remaining linear features are

292   secondary crater chains formed by material ejected from nearby and distant impact craters. The

293   Samhain Catenae's spacing indicates that Ceres' outer layer in their vicinity is approximately

294   ≥58 km thick. This is at least ~14 km thicker than the global average. It is also consistent with

295   gravity-derived interior model estimations of variations in the outer layer thickness [*Ermakov et*

296   *al.,* in revision], and thus provides independent confirmation for this model. Additionally, we

297   hypothesize that the Samhain Catenae were formed as the result of a region of upwelling

298   material derived from convection or diapirism. We find the characteristics of this proposed

299   region of upwelling material, which can be used as constraints in future modeling studies of

300   Ceres' interior evolution. For example, we approximate its location to be ~36°N, ~207°E. This

301   broadly coincides with Hanami Planum, which is a topographically high region with a negative

302   residual gravity anomaly. A subsurface buoyancy-driven anomaly combined with a high

303   rigidity/thick outer layer is one possible formation mechanism of Hanami Planum [*Ermakov et*

304   *al.,* in revision]. Consequently, Hanami Planum may be evidence for the proposed region of

305   upwelling material, and the Samhain Catenae may represent surficial evidence for past interior

306   activity.

307

308

309

310 **Acknowledgments, Samples, and Data**

320

321 **References**

322 Bai, T. and Pollard, D. D. (2000), Fracture spacing in layered rocks: a new explanation based on

323   the stress transition, *J. Struct. Geol.*, *22*, 43-57.

324 Bland, M. T. (2013), Predicted crater morphologies on Ceres: Probing internal structure and

325   evolution, *Icarus, 226*, 510-521.

326 Bland, M. T., and McKinnon, W. B. (2015), Forming Ganymede's grooves at smaller strain:

327   Toward a self-consistent local and global strain history for Ganymede, *Icarus, 245,* 247-

328   262.

329 Bland, M. T., et al. (2016), Composition and structure of the shallow subsurface of Ceres

330   revealed by crater morphology, *Nat. Geosci., 9,* 538-542.

331 Buczkowski, D. L., Barnouin-Jha, O. S. and Prockter, L. M. (2008), 433 Eros lineaments: Global

332   mapping and analysis, *Icarus*, *193,* 39-52.

333   Buczkowski, D. L., et al. (2016), The geomorphology of Ceres, *Science, 353 (6303)*, 1004.

334   Castillo-Rogez, J. C. and McCord, T. B. (2010) Ceres' evolution and present state constrained by

335   shape data, *Icarus, 205*, 443-459.

336   Castillo-Rogez, J. C., et al. (2016), Loss of Ceres' Icy Shell from Impacts: Assessment and

337   Implications, *Lunar Planet. Sci. Conf.*, *47*, 3012.

338   De Sanctis, M. C., et al. (2015), Ammoniated phyllosilicates with a likely outer Solar System

339   origin on (1) Ceres, *Nature*, *528*, 241-244.

340   Drummond, J. D., et al. (2014), Dwarf planet Ceres: Ellipsoid dimensions and rotational pole

341   from Keck and VLT adaptive optics images, *Icarus, 236*, 28-37.

342   Ermakov, A. I., et al. (in revision), Constraints on Ceres' internal structure and evolution from its

343   shape and gravity measured by the Dawn spacecraft, *J. Geophys. Res*. *This manuscript

344   is included with this submission. We expect it would be published before this paper

345   would be accepted but if it were not, we would substitute this reference with a 2017

346   LPSC abstract on the same topic.

347   Ernst, R. E., and Buchan, K. L. (2001), The use of mafic dike swarms in identifying and locating

348   mantle plumes, *Geological Society of America*, Special Paper 352.

349   Ferrill, D. A., Wyrick, D. Y. and Smart, K. J. (2011), Coseismic, dilational-fault and extension-

350   fracture related pit chain formation in Iceland: Analog for pit chains on Mars,

351   *Lithosphere*, *3,* 133-142.

352   Fu, R. R., et al. (in revision), The Interior Structure of Ceres as Revealed by Surface

353   Topography, *Earth Planet. Sc. Lett.* *This manuscript is included with this submission.

354   We expect it would be published before this paper would be accepted but if it were not,

355   we would substitute this reference with a 2016 AGU abstract on the same topic.

356   Gioia, G., Chakraborty, P., Marshak, S. and Kieffer, S. W. (2007), Unified model of tectonics

357   and heat transport in a frigid Enceladus, *P. Natl. Acad. Sci.*, *104,* 13578-13581.

358   Hiesinger, H., et al. (2016), Cratering on Ceres: Implications for its crust and evolution. *Science*,

359   *353,* aaf4759-1-8.

360   King, S. D., et al. (2016), 3D Spherical Convection Modeling of the Interior of Ceres, *Lunar*

361   *Planet. Sci. Conf., 47,* 1699.

362   Lange, M. A. and Ahrens, T. J. (1983), The Dynamic Tensile Strength of Ice and Ice-Silicate

363   Mixtures, *J. Geophys. Res., 88*, 1197-1208.

364   Li, J.-Y., et al. (2006), Photometric analysis of 1 Ceres and surface mapping from HST

365   observations, *Icarus*, *182,* 143-160.

366   Longobardo, A., et al. (2015), Mineralogical and spectral analysis of Vesta's Gegania and

367   Lucaria quadrangles and comparative analysis of their key features, *Icarus, 259*, 72-90.

368   Manga, M. and Wang, C.-Y. (2007), Pressurized oceans and the eruption of liquid water on

369   Europa and Enceladus, *Geophys. Res. Lett.*, *34*, L07202-1-5.

370   Marchi, S., et al. (2016), The missing large impact craters on Ceres, *Nat. Comm., 7 (12257)*, 1-9.

371   Martin, E. S., et al. (2017), Pit chains on Enceladus signal the recent tectonic dissection of the

372   ancient cratered terrains, *Icarus, 294,* 209-217.

373   McCord, T. B. and Sotin, C. (2005), Ceres: Evolution and current state. *J. Geophys. Res., 110*,

374   E050091-1-14.

375   Mitri, G., et al. (in revision), Crustal Structure and Internal Differentiation of the Dwarf Planet

376   Ceres, *Icarus*. *This manuscript is included with this submission. We expect it would be

377   published before this paper would be accepted but if it were not, we would substitute this

378   reference with a 2017 EGU abstract on the same topic.

379   Neveu, M. and Desch, S. J. (2015), Geochemistry, thermal evolution, and cryovolcanism on

380   Ceres with a muddy ice mantle, *Geophys. Res. Lett.*, *42*, 10197-10206.

381   Nimmo, F. (2004), Stress generated in cooling viscoelastic shells: Application to Europa, *J.*

382   *Geophys. Res., 109,* E12001-1-10.

383   O'Brien, D. P., et al. (2015), The Potential for Volcanism on Ceres Due to Crustal Thickening

384   and Pressurization of a Subsurface Ocean, *Lunar Planet. Sci. Conf.*, *46,* 2831.

385   Park, R. S., et al. (2016), A partially differentiated interior for (1) Ceres deduced from its gravity

386   field and shape, *Nature, 537,* 515-517.

387   Petrovic, J. J. (2003), Review – Mechanical properties of ice and snow, *J. Mater. Sci.*, *38*, 1-6.

388   Preusker, F., et al. (2016), Dawn at Ceres – Shape Model and Rotational State, *Lunar Planet. Sci.*

389   *Conf.*, *47*, 1954.

390   Roatsch, Th., et al. (2016), High-resolution Ceres High Altitude Mapping Orbit atlas derived

391   from Dawn Framing Camera images, *Planet. Space Sci., 129*, 103-107.

392   Russell, C. T., et al. (2016), Dawn arrives at Ceres: Exploration of a small, volatile-rich world,

393   *Science*, *353*, 1008-1010.

394   Schmedemann, N., et al. (2017), The Distribution of Impact Ejecta on Ceres, *Lunar Planet. Sci.*

395   *Conf., 48,* 1233.

396   Scully, J. E. C., et al. (2014), Geomorphology and structural geology of Saturnalia Fossae and

397   adjacent structures in the northern hemisphere of Vesta, *Icarus, 244,* 23-40.

398   Thomas, P. C., et al. (2005), Differentiation of the asteroid Ceres as revealed by its shape,

399   *Nature, 437,* 224-226.

400   Travis, B. J. and Feldman, W. C. (2016), Ceres Model Suggests Large Scale Topography May

401   Reflect Early Time Internal Convection, *Lunar Planet. Sci. Conf.*, 47, 2762.

402   Wyrick, D., et al. (2004), Distribution, morphology, and origins of Martian pit crater chains, *J.*

403   *Geophys. Res., 109,* E06005-1-20.

404   Yin, A., et al. (2016), Mechanics of evenly spaced strike-slip faults and its implications for the

405   formation of tiger-stripe fractures on Saturn's moon Enceladus, *Icarus*, *266,* 204-216.

406   Zolotov, M. Y. (2009), On the composition and differentiation of Ceres, *Icarus*, *204,* 183-193.